

Microphysical modes of precipitation growth determined by S-band vertically pointing radar in orographic precipitation during MAP

By SANDRA E. YUTER* and ROBERT A. HOUZE JR
University of Washington, Seattle, USA

(Received 28 December 2001; revised 12 July 2002)

SUMMARY

High-resolution vertically pointing S-band Doppler radar data obtained within orographic rain by the University of Washington Orographic Precipitation Radar (OPRA) at Locarno-Monti, Switzerland during the Mesoscale Alpine Programme (MAP) Intensive Observing Periods (IOPs) 2b and 8 are examined to characterize the fine-scale precipitation structure. The relative roles of collection of cloud water by raindrops versus collection of cloud water by ice particles (riming) in the same column are assessed with a one-dimensional (1D) Kessler water-continuity model using the observed data characteristics as input.

The OPRA data reveal nearly ubiquitous small-scale fallstreaks each <5 minutes in duration occurring within a wide range of precipitation intensities. Periods of higher rain rates >10 minutes in duration associated with convective cells evident in coarser-resolution data manifested as increased frequency and intensity of fallstreaks in the OPRA data. A subset of fallstreaks had sufficient magnitude in reflectivity to indicate a clear connection from the snow region, across the melting layer and into the rain region. The small-scale inhomogeneities in microphysical structure associated with fallstreaks are likely to be associated with convective overturning in the unstable IOP 2b case. In the more stable IOP 8 case, shear-driven turbulence near the melting layer, evident in truck-borne and airborne X-band Doppler-radar data shown in companion studies, is a likely contributor to fallstreak formation.

The vertical profile of vertical air velocity (w) is critical to understanding the relationship between collection and riming, and their contributions to precipitation efficiency. Characteristics of the w profile within precipitating cloud were estimated in both rain and snow using observed radar parameters from the OPRA data. In rain, reflectivity-weighted fall speed was derived from observed reflectivity and assumptions about the raindrop size distribution. The derived fall velocity was subtracted from the observed Doppler radial velocity to estimate w in rain regions to within $\sim 1.5 \text{ m s}^{-1}$. In snow regions, a lower bound on peak updraught velocity was estimated from the observed maximum Doppler velocity. For the data examined from MAP IOP 2b, typical peak updraught velocities at Locarno-Monti were between 2 and 5 m s^{-1} .

These estimated peak updraught velocities were used to construct plausible parabolic profiles of w that were in turn used as input to a 1D Kessler water-continuity model. Model output shows local maxima in the riming rate and mixing ratio of ice within 2 km of the freezing level, indicating a favourable environment for graupel formation. The location of this layer in the model is consistent with the observed occurrence of graupel in National Center for Atmospheric Research S-Pol radar data in the IOP 2b storm in a companion study. The modelled rates of collection and riming are comparable, and both make significant contributions to the growth by accretion of precipitation within the storm updraughts. Within the rain layer, liquid-water coalescence (autoconversion and collection) in updraughts with peak velocities of 5 m s^{-1} can account for up to $\sim 40\%$ of column-integrated cloud water.

Our analysis of the observational data and the 1D model results confirms and extends previous work indicating that a combination of liquid-water coalescence and ice-phase processes is needed to obtain high precipitation efficiencies >40% in orographic precipitation.

KEYWORDS: Accretion Fallstreaks Mesoscale Alpine Programme One-dimensional water-continuity model Riming

1. INTRODUCTION

Heavy rain of the type that causes flooding in the Alps is produced both quickly and efficiently over the lower slopes of the Alpine barrier. Cloud water condensed over the terrain is swept out rapidly by precipitation particles. Terminology from water-continuity models describes the modes of rapid precipitation growth by the accretion of liquid cloud water below the freezing level as *collection* of cloud water by raindrops, and the collection of cloud water by ice particles above the 0°C level as *riming* (Houze 1993). By understanding the relative roles of collection and riming better, we expect

* Corresponding author: Atmospheric Sciences, Box 351640, University of Washington, Seattle, WA 98195-1640, USA. e-mail: yuter@atmos.washington.edu

TABLE 1. CHARACTERISTICS OF THE UNIVERSITY OF WASHINGTON OROGRAPHIC PRECIPITATION RADAR (OPRA) DURING MAP

Model	Modified Raytheon Pathfinder S-band
Receiver	NCAR/ATI PIRAQ
Signal Processor	50 MHz TI TMS320C50 on PIRAQ board
Host Computer	233 MHz Pentium II MMX, 32 MB RAM, 4 GB disk, DAT, CDROM
Frequency	3050 MHz
Antenna	1.8 m offset-feed parabola
Antenna Gain	31 dB (estimated)
Antenna Height	382 m a.m.s.l.
Transmitter	Magnetron, 2J75B with solid state modulator
Peak Power	60 kW maximum, 35 kW minimum
Beam Width	4.3° (estimated)
PRF	1000 Hz
Pulse Width	1.0 μ s
# Gates	100
Variables	Z , V_r , and spectral width (SW)



Figure 1. The University of Washington Orographic Precipitation Radar, OPRA, on the roof of the Swiss Meteorological Institute Osservatorio Ticinese in Locarno, Switzerland. The antenna has an offset feed and is set so the radar beam is pointing vertically. The radar's electronics, display and processing systems are contained within the small shelter to the left of the antenna.

to be able to improve modelling and prediction of heavy orographic rain events and to quantify their precipitation efficiency.

This paper assesses the relative roles of riming and collection in the same column of precipitating cloud using data from vertically pointing radar obtained during the Mesoscale Alpine Programme (MAP; Houze *et al.* 1998; Bougeault *et al.* 2001). The University of Washington Orographic Precipitation Radar (OPRA) is a vertically pointing 10 cm meteorological pulsed Doppler radar (Table 1). OPRA was deployed on the roof of the Swiss Meteorological Institute Osservatorio Ticinese from September to October 1999 at Locarno-Monti in Locarno, Switzerland, in collaboration with Jürg Joss and Urs Germann of the Swiss Meteorological Agency (SMA; Fig. 1). Approximately 365 hours of radar data were obtained during 11 of the MAP Intensive Observation

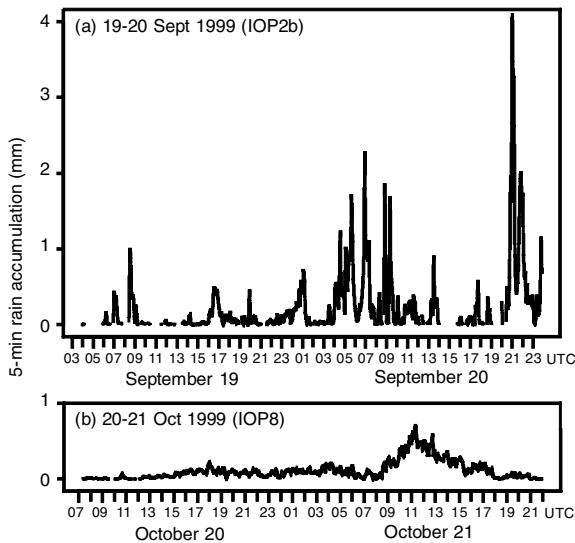


Figure 2. Time series of 5-minute rain accumulations from the Deutschen Zentrum für Luft und Raumfahrt disdrometer collocated with the University of Washington Orographic Precipitation Radar during (a) IOP 2b, and (b) IOP 8. (Data courtesy of Martin Hagen.)

Periods (IOPs). These data were taken on the lower windward slope of the Alps in a region of copious autumn rain and should represent precipitation mechanisms critical to Alpine orographic rainfall.

Previous studies have assigned a dominant precipitation growth process to particular time periods of data from vertically pointing radar. Wüest *et al.* (2000) classified the degree of riming over 30-minute periods using Formvar data of ice particles obtained concurrently with data from vertically pointing radar. White *et al.* (2001) classified the precipitation growth mechanism in 30-minute blocks of data from vertically pointing radar using the mean vertical profile of reflectivity and the presence or absence of a radar bright band. We approach the problem from a different perspective by addressing the relative contributions of riming and collection within the same column via vertical velocity measurements at 1 s time-resolution.

The vertical profile of the vertical velocity of air (w) is critical to understanding the relationship between collection and riming. We first estimate characteristics of the vertical profile of w using the observed Doppler velocity (V_r) data, and reflectivity-weighted fall speeds ($\langle V_t \rangle$, where subscript t is terminal velocity) derived from observed reflectivity (Z). From a profile of estimated w with height, we then use Kessler's one-dimensional (1D) water-continuity model (Kessler 1969) to assess the relative rates of accretion of cloud water in regions above and below the 0 °C level.

In this study, we focus on data obtained during 19–20 September 1999 (IOP 2b) and 20–21 October 1999 (IOP 8). The two cases represent contrasting stability and wind environments at levels below 900 hPa (see Medina and Houze (2003) for a discussion of the synoptic mesoscale settings for these cases, and Rotunno and Ferretti (2003) for mesoscale model simulations). IOP 8 was stable and relatively cool compared to the mean MAP sounding, and had weak winds from the surface to 900 hPa; IOP 2b was potentially unstable, warmer than the mean sounding and had strong winds at low levels. In both cases, above 900 hPa there were strong south-easterly winds toward the

Alpine barrier. The layer of flow toward and over the terrain in IOP 2b was deeper and more unstable than in IOP 8. The time series of 5-minute rain rates* reported by the Deutschen Zentrum für Luft und Raumfahrt (DLR) disdrometer at Locarno-Monti are shown in Fig. 2. During IOP 2b the rainfall was heavier and more variable (mean = 2.9, standard deviation = 5.5, maximum = 49, all mm h^{-1}) compared to the steadier rainfall in IOP 8 (1.4, 1.5, and 8.6 mm h^{-1} , respectively).

2. DATA

The OPRA data† consist of vertical profiles of radar reflectivity, Doppler radial velocity, and spectral width obtained every second at 150 m vertical resolution to a height of ~ 7 km‡. Horizontal beam width varies linearly as a function of height, from 75 m at 1 km to 525 m at 7 km. Consecutive 1 s profiles are not independent. For typical advection speeds of 3 to 10 m s^{-1} , the resulting horizontal advection of the precipitation structures is 3 to 10 m for a 1 s profile. For the analysis in this paper, a threshold value of autocorrelation at first lag (Bringi and Chandrasekar 2001, Eq. 5.195) was applied to remove bad Doppler velocity data. A more rigorous quality control procedure that will address side-lobe echo from the mountains across the Lago Maggiore valley is under development. When present, the side-lobe contamination in the OPRA data usually occurs at ~ 1.5 km altitude.

Figure 3 shows 45 minutes of OPRA data obtained during IOP 2b on 20 September 1999. From 0705 to 0725 UTC a region of heavy precipitation is indicated by the strong reflectivity values in rain and snow. The 0°C level is at ~ 3.5 km altitude. Fallstreaks are evident both above the 0°C level within snow and below within rain. A 300–500 m deep layer of enhanced reflectivities is associated with melting particles in the heavy precipitation. After 0725 UTC the convection weakens, and lighter precipitation falls until the end time of the plot at 0750 UTC (Figs. 3(a) and (c)). During the weaker precipitation portion of the 45-minute example, the layer of enhanced reflectivities associated with the melting of snow is narrower and slightly weaker than during the heavier precipitation periods. The high-resolution OPRA data reveal nearly ubiquitous small-scale fallstreaks in a wide range of intensities of precipitation. Fallstreaks in rain appear to originate in locally intense reflectivity regions within the melting layer and may connect to a fallstreak in snow descending from above.

The high-resolution data obtained by OPRA can be put into the context of the larger-scale precipitation system by examining data collected by two scanning radars utilized during MAP: the Swiss Meteorology Agency C-band radar at Mt. Lema 16 km south-east of OPRA, and the National Center for Atmospheric Research (NCAR) S-Pol radar 52 km south of OPRA (Fig. 4(a)). Both scanning radars were blocked by topography from scanning near the surface at OPRA's position. Figure 4(a) shows the mesoscale reflectivity field at 0718 UTC 20 Sept 1999, during the period of heavy rainfall shown in Fig. 3. The intense precipitation over OPRA was one of many localized regions of heavy precipitation associated with the interaction of the large-scale south-easterly

* Rainfall rates were recorded every minute but are shown as accumulations every 5 minutes to reduce measurement uncertainty associated with the small sample volume of the instrument. To convert to equivalent mm h^{-1} multiply the 5-minute accumulation by 12.

† Urs Germann of SMA compared the OPRA reflectivity data to the continuously calibrated SMA Mt. Lema C-band radar data. He found spatially and temporally coincident samples to be within a few dB of one another. This agreement is as close as can be expected considering the differences in sample volume sizes.

‡ All heights are above ground level unless otherwise indicated.

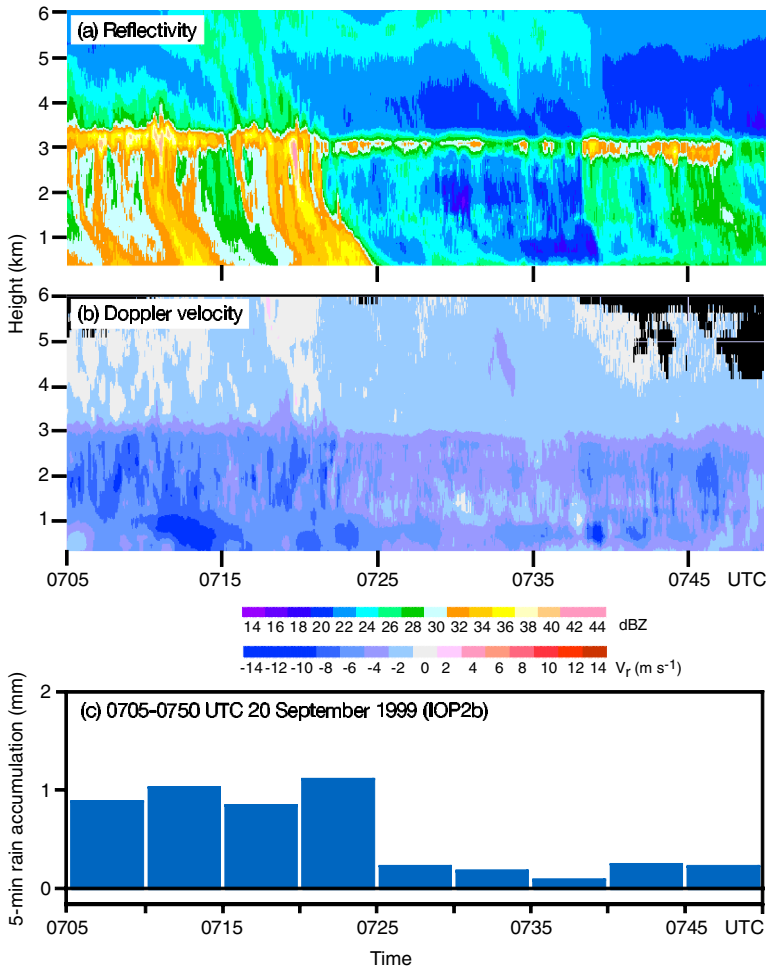


Figure 3. Time–height profiles for 45 minutes of 1 s data from the University of Washington Orographic Precipitation Radar (2700 profiles) from 0705–0750 UTC 20 Sept 1999 during IOP 2b: (a) radar reflectivity (Z), (b) Doppler velocity (V_r), (c) 5-minute rain accumulations from the Deutschen Zentrum für Luft und Raumfahrt disdrometer. The reflectivity data shown are the raw data as observed. Heights are a.m.s.l. The mean surface rain-rate is 6.4 mm h^{-1} and the maximum is 13.3 mm h^{-1} .

flow and the Alps (Frei and Schär 1998; Houze *et al.* 2001). The location of the precipitation relative to the topography is best shown by the north–south cross-section in Fig. 4(b). Reflectivity and precipitation maxima are associated with upslope regions of the topography. The operational scan strategy for Mt. Lema is optimized to obtain high-resolution time data of the near-surface reflectivity, and repeats every 5 minutes. The S-Pol radar used a research scan strategy to yield high-resolution spatial data, and scanned slower and to higher elevations than the Mt. Lema radar. A detailed analysis of the NCAR S-Pol radar data for IOPs 2b and 8, including dual-polarization data, is presented in Medina and Houze (2003).

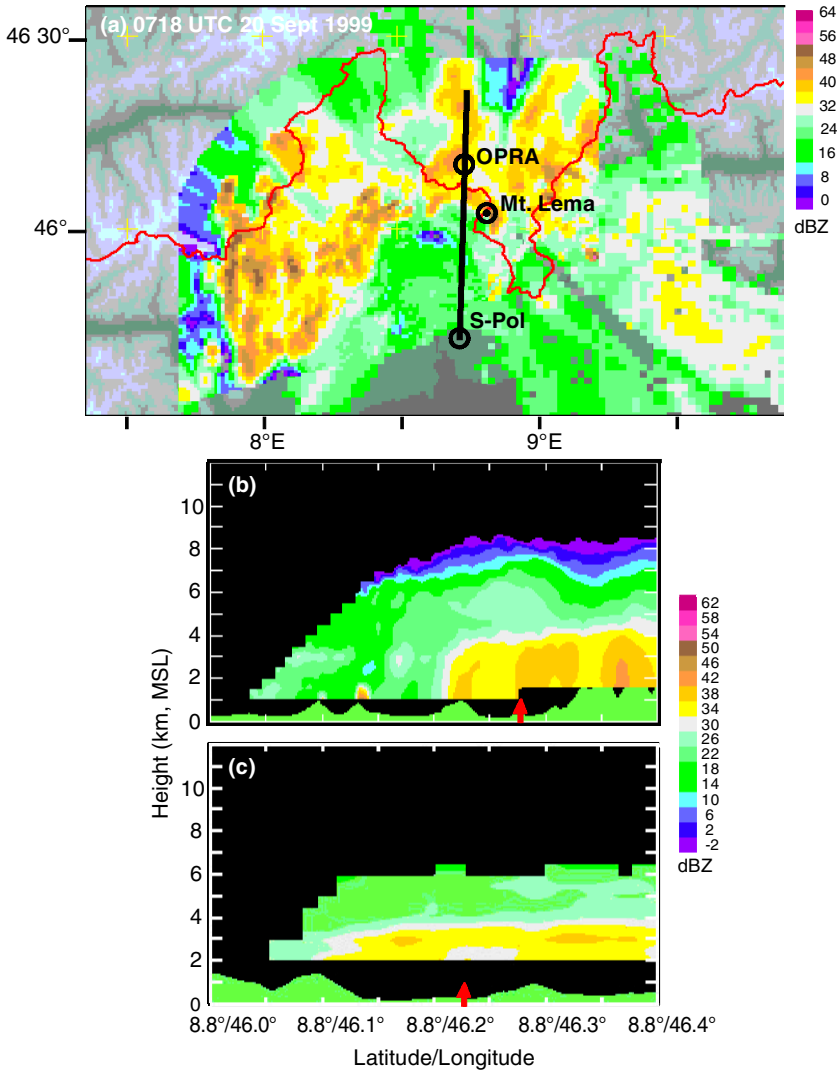


Figure 4. (a) Overlapped horizontal cross-sections of radar reflectivity at 2 km a.m.s.l. from the Swiss Meteorological Agency Mt. Lema C-band radar and the NCAR S-Pol radar for 0718 UTC 20 Sept 1999. The red line indicates the international border between Switzerland and Italy. (b) Vertical cross-section through topography (solid green) and S-Pol radar reflectivity data along a roughly south–north line from S-Pol to the University of Washington Orographic Precipitation Radar (OPRA); the reflectivity enhancements near the top of the first and second peaks from the left are side-lobe contamination. (c) Vertical cross-section through topography (solid green) and Mt. Lema radar reflectivity data along line (not shown) from Mt. Lema to OPRA. In (b) and (c) the location of OPRA is shown by the red arrow.

3. STRUCTURES AND SCALES OF PRECIPITATION VARIATION

It is well known that precipitation varies at small space- and time-scales. Waldvogel (1974) examined the minute-to-minute variation of raindrop size distribution (RDSD, drops >0.3 mm diameter) characteristics derived from disdrometer data in the context of vertically pointing C-band radar. Joss and Gori (1978) showed that the characteristics of the RDSD varied with scale and tended to converge toward an exponential character for longer time periods of several hundred minutes. They hypothesized that precipitation

at the scale of a typical scanning radar volume ($\sim 1 \text{ km}^3$) consisted of a mixture of rain rates of different intensities. Jameson and Kostinski (2000) examined drop size distribution time series and discussed the clustering of raindrops which could potentially physically interact over time periods as short as 2–3 s. They hypothesized that typical observed distributions (usually at least 1 minute in duration) represent probability mixtures of many short-duration spectra. Building on this previous work, OPRA provides an opportunity to examine the time–height variation of precipitation at up to 1 s time-resolution.

Gossard *et al.* (1990) describe the ambiguity in interpreting data from vertically pointing radar in terms of several generic structures: time-varying horizontal sheets, time stationary vertical shafts, and tilted shafts translated over the radar by the horizontal wind. Combinations of these structures appear likely in the OPRA data examined, with the melting layer often most similar to a time-varying sheet and fallstreaks most similar to vertical or tilted shafts depending on the vertical wind shear.

(a) *Fallstreaks and variations in fine-scale structures*

From the time series of surface precipitation in Fig. 2 one can filter out by eye the higher-frequency variations, and observe ‘pulses’ of heavier precipitation tens of minutes in duration and at least a factor of two greater than the background precipitation rate. These pulses are associated with the movement of locally intense regions within mesoscale precipitation systems as shown in Fig. 4(c).

The reflectivity and Doppler velocity structures* associated with some of these precipitation pulses can be observed in detail in Figs. 3 and 5 for IOP 2b, and in Figs. 6 and 7 for IOP 8. In Figs. 3 and 6 the pulses in precipitation intensity are associated with an increase in the frequency and intensity of fallstreaks, where individual fallstreaks are <5 minutes in duration (e.g. 0705–0725 and 0945–1030 UTC). The light-rain situation† in Fig. 7 exhibits similar fallstreak structures‡ but at reduced reflectivities compared to the other examples.

A precipitation fallstreak is a manifestation of an inhomogeneity in the microphysical structure of the storm. To be observed, the relative size and number of precipitation particles within the fallstreak need to be sufficient such that their radar reflectivity stands out as a local maximum from the immediate background reflectivities. The temporal and spatial resolution of the observing instrument determine whether a particular spatial-scale inhomogeneity in the microphysical structure can be observed. For a discrete precipitation inhomogeneity to be clearly resolved as a fallstreak, the time-resolution of the data should be less than the time it takes the set of precipitation particles to fall through an individual range gate§ and the horizontal resolution of an individual range gate has to be smaller than the size of the inhomogeneity.

Fallstreaks can develop as a result of one of several dynamical processes or their combination: buoyant convective overturning of saturated air associated with discernible

* Similar to data from other vertically pointing radars, the tilt of features in the OPRA time–height reflectivity plots is a function of both the horizontal advection speed and the fall speed of the precipitation particles. For a given fall speed, the lower the horizontal advection speed of the features over the radar, the larger the slope of the features in the graph.

† The apparent lack of relation between the near-surface reflectivities and the rain rates in the light-rain case in Fig. 7 is likely to be a result of the larger uncertainty in rain rate associated with a smaller total number of raindrops per 5-minute sample (Smith *et al.* 1993).

‡ These structures are more apparent when the reflectivity colour-scale is modified to better represent the lower range of reflectivities (not shown).

§ In the OPRA data, a raindrop falling at 8 m s^{-1} will take 18.75 s to fall through a 150 m range gate.

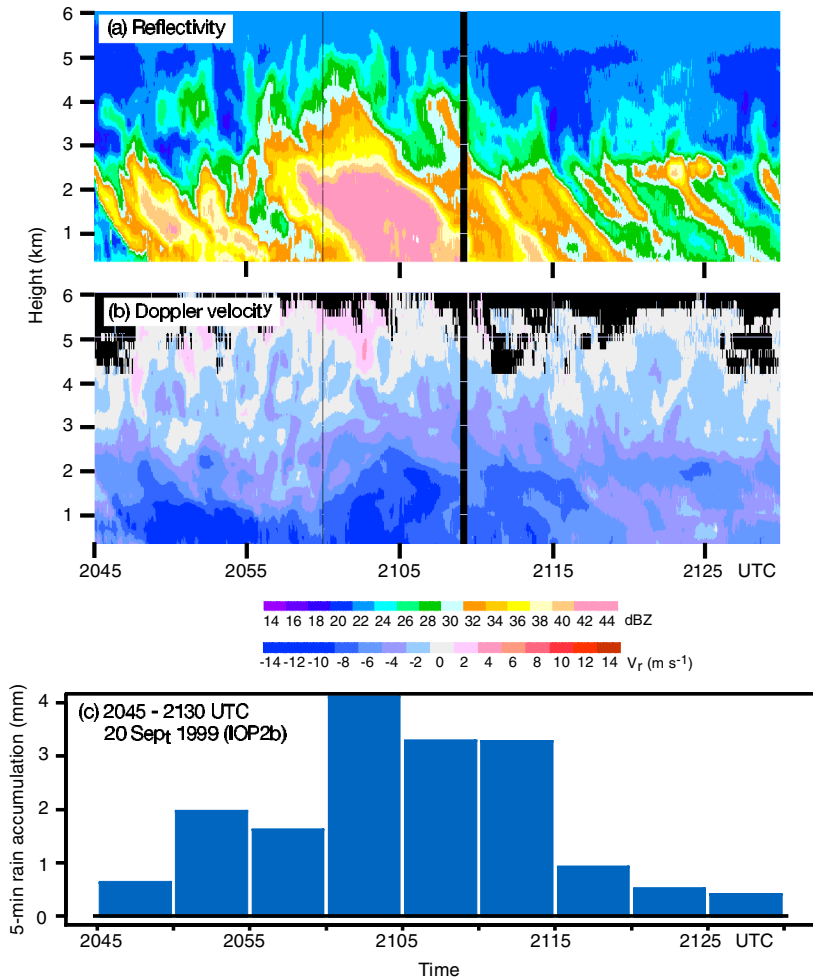


Figure 5. Same as Fig. 3 except for 2045–2130 UTC 20 September 1999 during IOP 2b. The surface rain-rate mean is 22.3 mm h^{-1} and the maximum is 49.2 mm h^{-1} .

updraughts, shear-driven turbulence, and convective overturning within the melting layer. In a recent combined aircraft and scanning-radar study, Hogan *et al.* (2002) related shear-driven turbulence in the form of Kelvin–Helmholtz instability near the melting layer to ~ 1 km-scale microphysical variability associated with embedded convection within a warm-frontal mixed-phase cloud. During the unstable IOP 2b storm, buoyant convective overturning is likely to have been the dominant mechanism producing fallstreaks. In IOP 8, strong shear was observed near the 0°C level (Steiner *et al.* 2003) in valley flows. Within the stable conditions of the IOP 8 storm, fallstreaks probably developed primarily as a result of shear-driven turbulence.

In Fig. 5 fallstreaks < 5 minutes in duration are discernible except during the heavy-rain period ($> 36 \text{ mm h}^{-1}$) from 2100–2110 UTC. The Doppler velocity measurement of 4 m s^{-1} at 4.5 km altitude at 2102 UTC represents a lower limit on the updraught velocity, and is an indirect indicator of convective overturning associated with a particularly vigorous updraught within the storm. Vigorous overturning would act to diffuse the signature of individual fallstreaks and make them less distinct. The frequency of

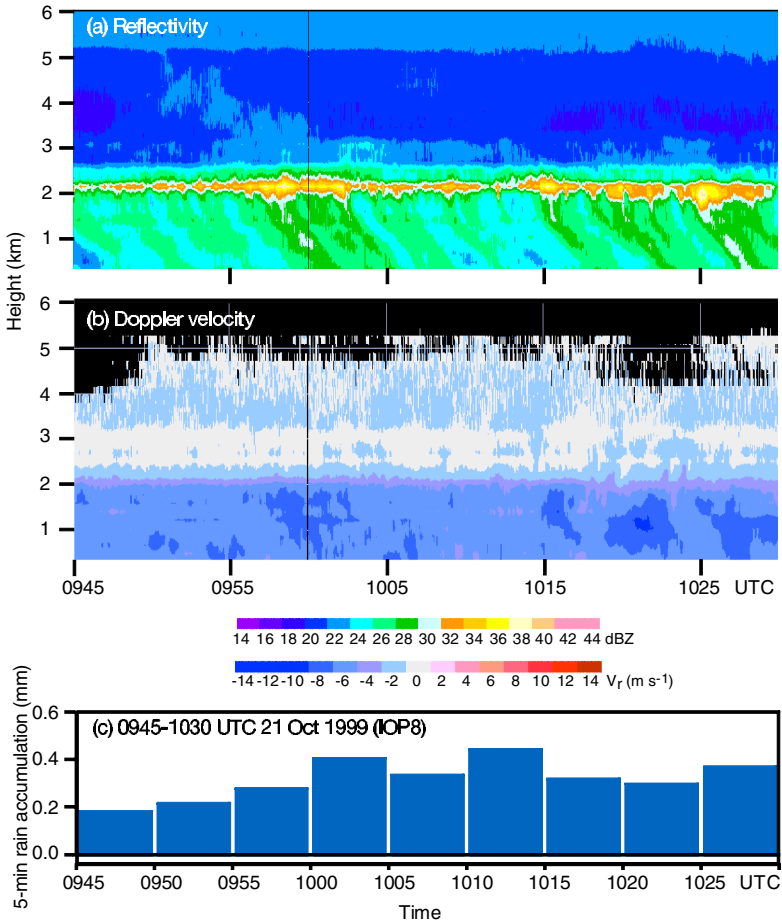


Figure 6. Same as Fig. 3 except for 0945–1030 UTC 21 October 1999 during IOP 8. The surface rain-rate mean is 3.8 mm h^{-1} and the maximum is 5.3 mm h^{-1} .

fallstreaks and their consistency in appearance over a wide range of rain rates indicates that they are an important small-scale precipitation structure in MAP precipitation.

(b) Melting layer

A distinct melting layer and associated strong gradient in Doppler velocity appears in Figs. 3(b) and 6(b) in terms of rain rates. Both these figures also include examples of fallstreaks in snow associated both with localized enhancements in reflectivity in the melting layer and with connected fallstreaks in rain. Although not readily apparent from the colour-scale used, the relative decrease in reflectivity from the melting band to peak reflectivities within fallstreaks 1 km below the melting band is similar (~ 8 – 10 dB) in both figures. For example, in Fig. 3 the local maxima of 42 and 44 dBZ within the melting layers at 0712 and 0720 UTC are associated with fallstreaks with peak reflectivities 1 km below the melting layers of 34 and 38 dBZ, respectively. Similarly, in Fig. 6, local maxima in the melting layer of 38 and 40 dBZ at 0958 and 1025 UTC are associated with peak reflectivities 1 km below the melting layer of 30 dBZ.

At the higher rain rates in Fig. 5 and the lower rain rates in Fig. 7 there is some evidence of a melting region (e.g. at 2120–2127 and 0547–0554 UTC, respectively)

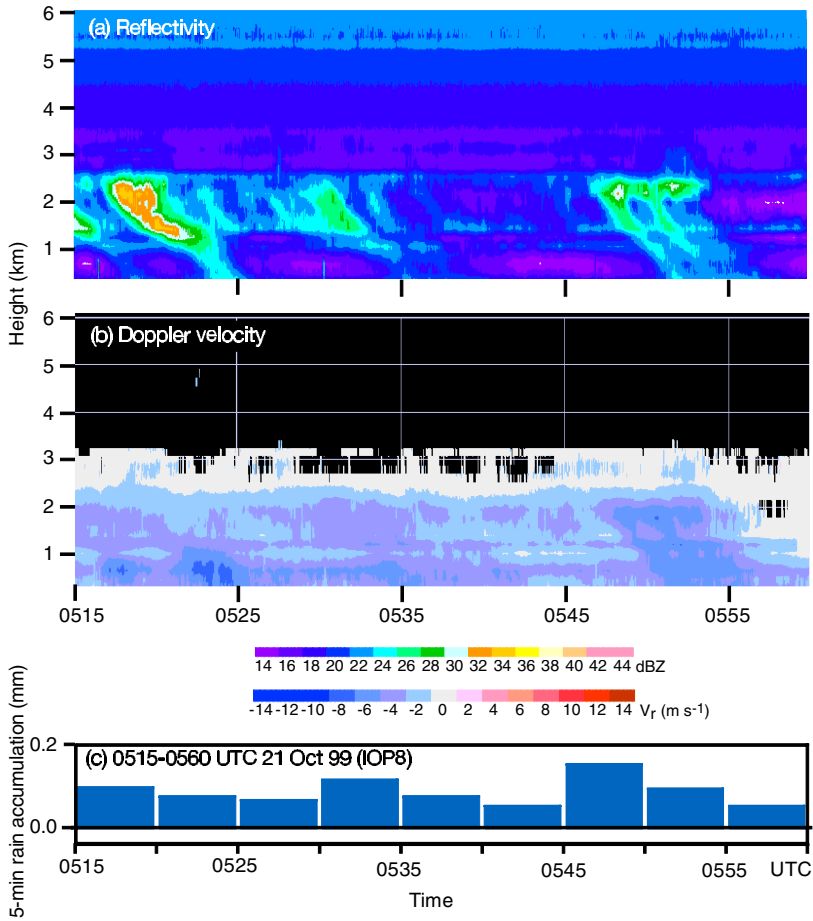


Figure 7. Same as Fig. 3 except for 0515–0560 UTC 21 October 1999 during IOP 8. The surface rain-rate mean is 1.0 mm h^{-1} and the maximum is 1.8 mm h^{-1} .

but a distinct melting layer is absent. In the light-rain case in Fig. 7 this can be easily explained by the minimal-to-absent radar echo at altitudes above the 0°C level and hence a lack of ice particles to melt. For the heavy-rain case in Fig. 5 the explanation is not as simple. Figure 5 clearly indicates precipitation particles above the freezing level. Ice nucleation arguments imply that it is unlikely that all the hydrometeors above the 0°C level are liquid, so melting of a portion of the hydrometeors must occur. Again, a possible explanation is that vigorous convective overturning would inhibit formation of a narrow well-defined melting layer. As the frozen portion of hydrometeors fell past the 0°C level they would melt over a deeper layer than in Fig. 3, and the radar ‘bright band’ enhancements associated with melting particles would be diffused over a greater depth (Yuter and Houze 1995).

4. ESTIMATION OF CHARACTERISTICS OF THE VERTICAL VELOCITY PROFILE IN SITUATIONS OF DOMINANT ACCRETIONAL GROWTH

In discriminating situations where growth by accretion is occurring, a subjective rain-rate threshold of 20 mm h^{-1} is often used, based on the physical argument that

vapour deposition processes by themselves cannot produce such high rain rates (Austin and Houze 1972; Churchill and Houze 1984). In the current study we do not need such a rigid condition. For the purpose of discriminating where dominant growth by accretion is likely to be (as opposed to definitely) occurring, we use as a guideline a rain rate of $\sim 10 \text{ mm h}^{-1}$, based on the finding of Steiner *et al.* (1995, their Fig. 9) of $\sim 10 \text{ mm h}^{-1}$ as the highest-frequency rain rate within convective precipitation observed at Darwin, Australia*. Following this general guideline, we focus our analysis in the next sections on portions of the IOP 2b storm with surface rain rates $\geq \sim 10 \text{ mm h}^{-1}$.

(a) *Derivation of vertical air velocity in rain*

The observed mean Doppler velocity represents the sum of the average air velocity and the mean reflectivity-weighted fall speed of the raindrops in the resolution volume ($V_r = w + \langle V_t \rangle$). If one knew the size distribution of the raindrops within the radar-resolution volume, one could apply an empirical diameter/fall-speed relation (e.g. Gunn and Kinzer 1949; Berry and Pranger 1974) using a suitable temperature and pressure to derive the distribution of fall speeds for the RDS. From that information one could compute the mean reflectivity-weighted fall speed for the RDS within the radar-resolution volume.

A basic practical problem with deriving w from V_r data is that the RDS in the radar-resolution volume is not directly measured. Methods are available to estimate some characteristics of the RDS from a recording of the full Doppler spectra (e.g. Gossard *et al.* 1990; Gossard 1998). However, OPRA was able to measure only the mean Doppler velocity values, as larger integration times are required to record a reliable full Doppler spectrum for each range gate.

The RDS can be represented as a gamma distribution following Ulbrich (1983) and Chandrasekar and Bringi (1987) by

$$dN = \frac{N_0}{m!} \Lambda^m D^m \exp(-\Lambda D) dD, \quad (1)$$

where D is drop diameter, Λ is the slope of the distribution $\Lambda = 6.12(W/Z)^{1/3}$, W is liquid-water content in units of $\text{mm}^3 \text{m}^{-3}$, and Z is radar reflectivity with units of $\text{mm}^6 \text{m}^{-3}$ (Waldvogel 1974). For desired values of rain rate, N_0 , and m , (1) can be iterated to determine the associated value of Λ . Specific forms of the distribution range from nearly monodisperse ($m = 16$) to exponential ($m = 0$). The sensitivity of estimates of $\langle V_t \rangle$ to assumptions regarding the values of N_0 and m in (1) is shown in Fig. 8 assuming a temperature of 10°C and pressure of 925 hPa (calculation provided by Jürg Joss, personal communication). The worst-case uncertainty† of $\sim 1.5 \text{ m s}^{-1}$ associated with the RDS assumptions is comparable to the uncertainty of aircraft *in situ* measurements of w .

Sets of Z and $\langle V_t \rangle$ values were calculated for different sets of assumptions regarding rain rate, m , and N_0 , and variations in temperature and pressure. These data were then fitted to an equation of the form:

$$\langle V_t \rangle = b + kZ, \quad (2)$$

* The rain rates in the Steiner *et al.* (1995) study were derived from $2 \text{ km} \times 2 \text{ km}$ horizontal-resolution radar reflectivity data. The differences in spatial resolution and precipitation climatology between the Steiner *et al.* study and the current study mean that the rain-rate values are unlikely to be directly comparable and hence are used as a general guideline.

† In applying the technique, errors associated with radar measurements of V_r and the calibration of Z will contribute additional uncertainty. Calibration errors would yield a systematic bias.

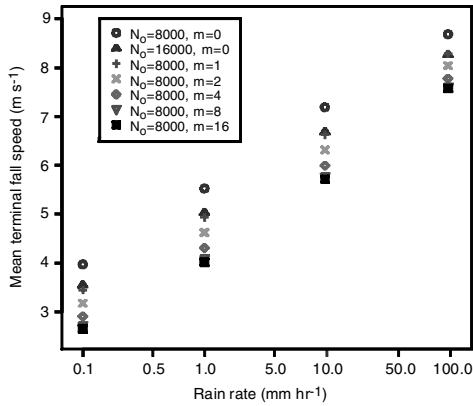


Figure 8. Estimated fall speed, V_t , as a function of rain rate and varying raindrop size distribution parameters N_0 and m (see text). The calculation was provided by J. Joss (personal communication).

where Z is in units of dBZ, in order to analytically determine the coefficients b and k as a function of m , N_0 , temperature and pressure. Turbulence is assumed to be symmetric such that over the radar-resolution volume its mean is zero.

This method of estimating $\langle V_t \rangle$ (Jürg Joss, personal communication) was applied to several samples of OPRA data. The lapse rate was assumed to be 6 K km^{-1} and the pressure decreased by a factor of $\exp(z/10)$ where z is height in km. The calculations were made assuming the RSD was exponential (i.e. $m = 0$), which is consistent with RSD observations at larger sample sizes approaching the scale of a radar volume (e.g. Joss and Gori 1978) and assigning $N_0 = 8000$ (Marshall and Palmer 1948). For these parameters the coefficients b and k are defined as follows, where temperature (T) is in Kelvin, and pressure (P) in hPa:

$$a = (T/P)^{0.45} + 0.3401, \quad (3)$$

$$k = 0.4099a + 0.00558/a, \quad (4)$$

$$b = -0.15 + 15.48a. \quad (5)$$

Figure 9 shows the method applied to OPRA data obtained from 0716 to 0721 UTC 20 Sept 1999. The observed Z field (Fig. 9(a)) was used to derive $\langle V_t \rangle$ (Fig. 9(c)); that, in turn, was combined with the observed V_r (Fig. 9(b)) to obtain w (Fig. 9(d)). Vertical velocity was estimated at each range gate in each radar data profile independently (i.e. no mass continuity constraint was applied).

A statistical representation of the derived w results is shown in Fig. 10(a) in terms of a contoured frequency by altitude diagram (CFAD; Yuter and Houze 1995), a joint frequency distribution of w with height. An abrupt shift in the modal values of w occurs at 2.75 km altitude near the bottom of the melting layer indicated by the dashed lines in Figs. 10(a) and (b). The method of estimating $\langle V_t \rangle$ is valid for the rain region below the melting layer. The CFAD shows that the strongest mode of the frequency distribution of w is near 0 m s^{-1} at all heights within rain ($< 2.7 \text{ km}$ altitude). This result is consistent with the frequency distribution of w based on studies of dual-Doppler data (e.g. Yuter and Houze 1995; Braun *et al.* 1997) and indicates that the bias in the method is small. Updraughts $< 3 \text{ m s}^{-1}$ predominate at low levels. The outliers of the distribution varied between approximately $+5 \text{ m s}^{-1}$ for updraughts and -6 m s^{-1} for downdraughts. Time–height plots of the estimated vertical velocity (Fig. 9(d)) indicate

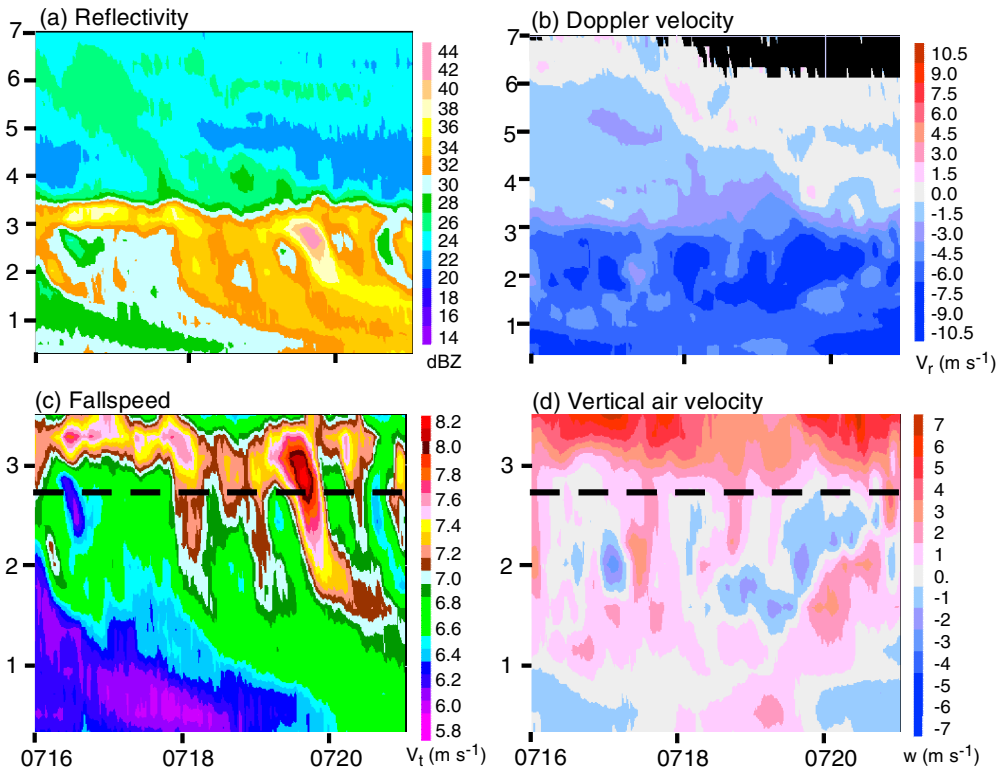


Figure 9. Example application of methodology to estimate vertical air velocity on 5 minutes of the University of Washington Orographic Precipitation Radar data from 0716–0721 UTC 20 September 1999. (a) Observed radar reflectivity (Z) to 7 km a.m.s.l., (b) observed Doppler velocity (V_r) to 7 km a.m.s.l., (c) derived fall speed (V_t) within the rain region, and (d) derived vertical air velocity (w) within the rain region. In (c) and (d) the melting layer between 3 and 3.5 km altitude is included to clarify its position. The methods to derive V_t and w are valid for the rain region below the ~ 2.75 km a.m.s.l. lower boundary of the mixed-phase region (indicated by the dashed lines in (c) and (d)).

coherent updraught and downdraught structures. The results of these simple tests are promising in that this method of deriving $\langle V_t \rangle$ produced physically realistic results. An alternate version of the fall speed and derived w fields were also obtained from the OPRA data using the Atlas *et al.* (1973) mapping of reflectivity to fall speed of $V_t = 2.6Z^{0.107}$. These w values yielded a distribution with a physically inconsistent negative bias (Fig. 10(b)).

(b) Derivation of vertical air velocity in snow

Ice crystals of different habits have different mass-to-size relationships, and hence different fall speed relations for the same diameter, temperature and pressure. Locatelli and Hobbs (1974) measured the fall velocities of a variety of snow particles of different crystal habits. Hanesch (1999) obtained relations between snow particles and fall speed for several degrees of riming using 2D-video disdrometer data obtained during the Swiss Alpine Melting Layer Measurements campaign in winter 1996–97. Both analyses found that most naturally occurring snow particles had fall speeds in still air from near 0 to 2 m s^{-1} and small graupel (5 mm diameter) had fall speeds of $\sim 3 \text{ m s}^{-1}$.

In order to estimate the fall speed of ice from reflectivity, a crystal habit and associated fall speed relation with size would need to be assumed. As a first step, a

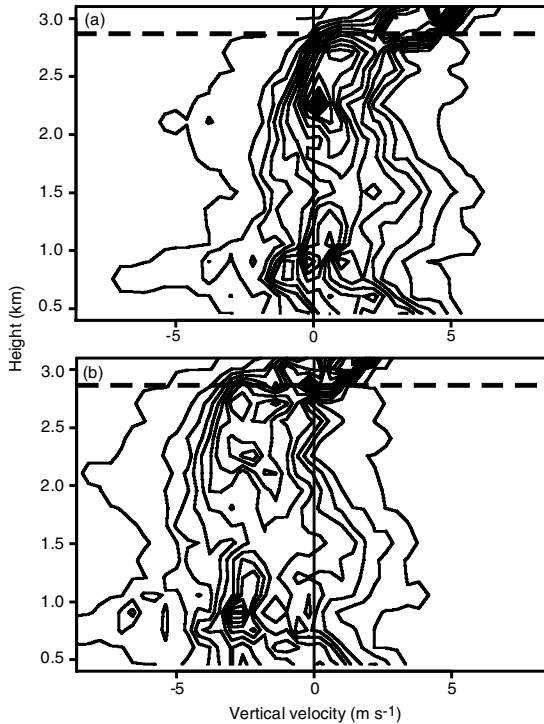


Figure 10. (a) Contoured frequency by altitude diagram (CFAD, Yuter and Houze 1995), of derived vertical air velocity, w , for data obtained from 0704–0750 UTC 20 September 1999. The joint frequency distribution is plotted using a w bin size of 0.2 m s^{-1} and height bin size of 150 m. (b) w derived using the Atlas *et al.* (1973) $Z - V_t$ formula (see text). A discontinuity (dashed line) is present in the plots at $\sim 2.75 \text{ km a.m.s.l.}$ where the transition from mixed phase to rain occurs. The derived w values are valid for the rain region below the dashed line.

simple method that does not require information about the particle size distribution is used to estimate a lower bound for the vertical air motions in snow. The observed Doppler velocity data in snow are split into two groups. For $V_r > 0 \text{ m s}^{-1}$, the observed Doppler velocity represents a robust underestimate of positive vertical air velocity. For $V_r \leq 0 \text{ m s}^{-1}$, the physical interpretation is ambiguous. One can examine the statistics of the underestimated positive vertical air velocities and interpret these velocities as characteristics of the vertical profile of w . For example, the maximum observed V_r of 2.2 m s^{-1} at 3.46 km altitude in Fig. 11 can be interpreted as a lower limit for maximum updraught velocities at this altitude for this sample. The use of measured V_r within snow and ice regions to estimate w can lead to an underestimate of w in these regions of up to the maximum fall speed of ice particles of $\sim 3 \text{ m s}^{-1}$.

Examination of estimated w below the 0°C level based on derived $\langle V_t \rangle$ in rain regions, and estimated lower bounds of maximum w above the 0°C level based on measurements of V_r in snow, yielded values of between 2 and 5 m s^{-1} for likely peak vertical velocities within typical* updraughts associated with precipitation at Locarno-Monti during IOP 2b. These velocities are assumed to occur as the local maximum within parabolic profiles of vertical velocity, which are in turn used as input to a 1D microphysical parametrization described below.

* The range $2\text{--}5 \text{ m s}^{-1}$ is intended to encompass those updraughts associated with a major portion of the precipitation accumulation in the IOP 2b storm.

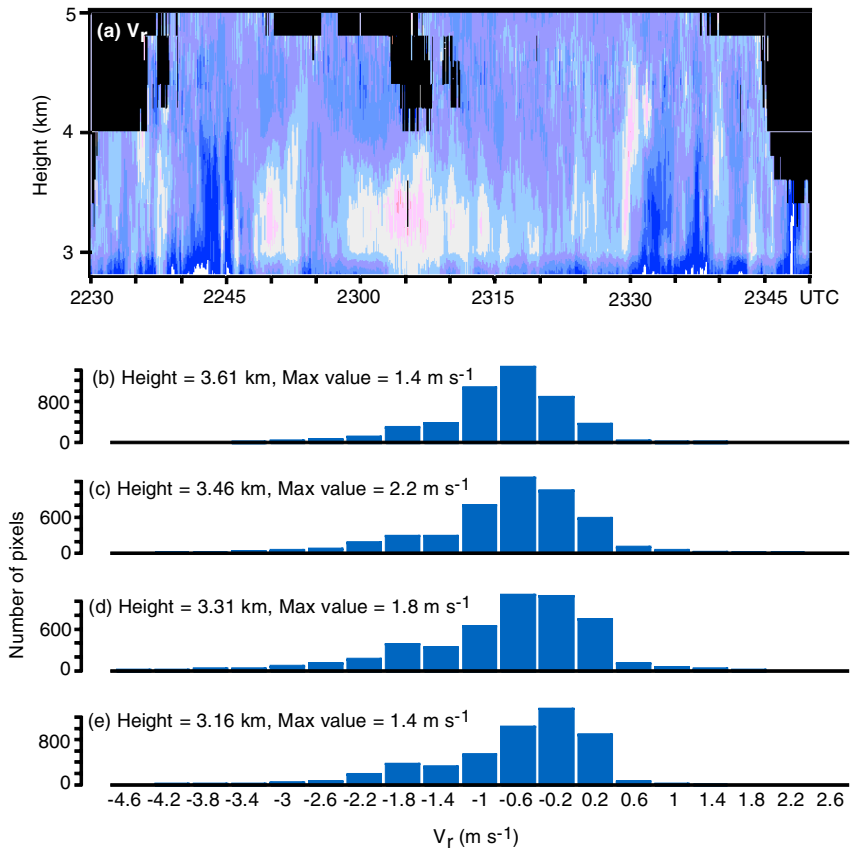


Figure 11. (a) Time–height profiles of the University of Washington Orographic Precipitation Radar Doppler velocity, V_r , data within the ice region and a portion of the melting layer for 2230–2350 UTC 19 September 1999. (b) Histogram of V_r values for layers 150 m deep at 3.61 km; (c), (d), and (e) as (b) but at 3.46 km, 3.31 km, and 3.16 km respectively. All heights are a.m.s.l.

5. RELATIVE ROLES OF DIFFERENT PROCESSES IN PRECIPITATION GROWTH

Precipitation growth by accretion occurs within updraughts. By simulating small-scale updraughts, typical of those embedded in the baroclinic rainstorms observed in MAP, with a 1D parcel model, we can determine the altitudes where condensate is available and the preferred layers for different particle growth processes. Since the small-scale updraughts occur within a broad layer of generally stratiform cloud and precipitation, growth occurs both on precipitation particles produced within the updraught and on pre-existing precipitation particles entrained into the updraught. The simple 1D parcel model below calculates only the former, but its results also indicate growth processes available to pre-existing particles.

(a) Adaptation of the Kessler 1D model

An estimation of the relative roles of several precipitation processes in the growth of precipitation was made using a simple 1D column-model calculation (Fig. 12) for a precipitating cold cloud following Kessler (1969), Ogura and Takahashi (1971), Ferrier (1988), and Houze (1993, section 3.6). The following equations describe water continuity in terms of the rate of change of the mixing ratios of water vapour (q_v), cloud

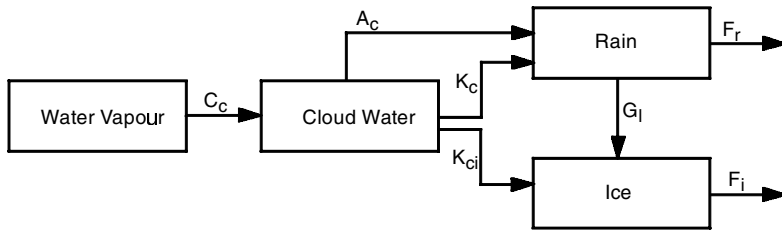


Figure 12. Block diagram of the Kessler 1D model. See text for explanation of symbols.

water (q_c), rain (q_r), and ice (q_i) in the 1D model:

$$\frac{Dq_v}{Dt} = -C_c, \quad (6)$$

$$\frac{Dq_c}{Dt} = C_c - A_c - K_c - K_{ci}, \quad (7)$$

$$\frac{Dq_r}{Dt} = A_c + K_c - F_r - G_1, \quad (8)$$

$$\frac{Dq_i}{Dt} = G_1 + K_{ci} - F_i, \quad (9)$$

where C_c is condensation of cloud water, A_c is autoconversion (the rate at which cloud water content decreases due to growth of precipitation by collision and coalescence of cloud drops), K_c is the collection of cloud water by raindrops, K_{ci} is the collection of cloud water by graupel above the 0°C level (i.e. riming), G_1 is the glaciation of rain into ice, F_r is the fallout of raindrops from the air parcel, and F_i is the fallout of ice particles.

The parcel is assumed to be saturated with respect to liquid water at all temperatures (i.e. entrainment and evaporation are ignored). Integration starts at cloud base ($z = 1$ km) where $q_c = q_v = q_i = 0$ and $q_v = q_{vs}$ the saturation mixing ratio. The calculation was performed using an altitude increment of 8 m for altitudes from 1000 to 7000 m. The lapse rate was set to 6 K km^{-1} and the temperature at 1000 hPa was set to 291 K based on Milan soundings for 20 September 1999. The fall speed of rain was set to 6 m s^{-1} and the fall speed for ice was set to a value for graupel of 3 m s^{-1} . Once the parcel is above the freezing level glaciation is assumed to be rapid, such that by ~ 1 km above the freezing level all the pre-existing rain has glaciated. Rapid glaciation is consistent with data obtained in several field studies (e.g. Yuter and Houze 1995; Zeng *et al.* 2001). The calculation is particularly sensitive to the assumptions regarding the glaciation rate and the fall speed relation of ice particles. See the appendix for further details on the model calculation.

(b) Model results

The 1D parcel model permits evaluation of changes in water vapour, cloud-water, rain and ice mixing ratios with height, and their associated precipitation processes, at a snapshot of time near the peak strength of an updraught whose characteristics are derived from MAP observations. Several runs of the 1D calculations were made using fixed parabolic profiles of vertical air velocity from 1 to 7 km altitude and from 1 to 5 km altitude, assuming a 0°C level at 3 km altitude. Figures 13 and 14 show the calculations for maximum w of 2 m s^{-1} for a velocity profile extending to 7 km altitude, and for maximum w of 5 m s^{-1} within a velocity profile extending to 5 km altitude.

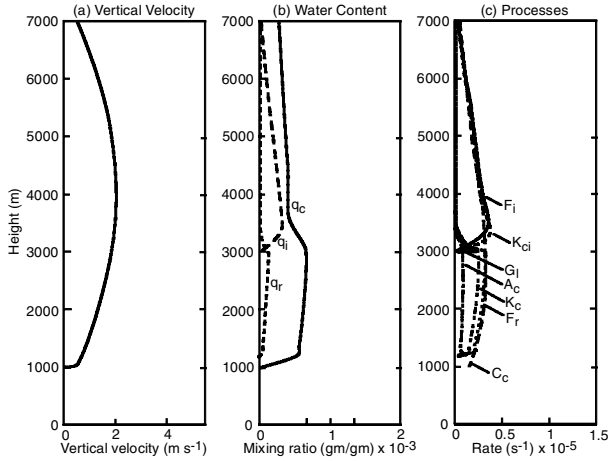


Figure 13. (a) Vertical velocity (w) profile with maximum $w = 2 \text{ m s}^{-1}$ and updraught top of 7 km a.g.l. used as input to Kessler 1D model. (b) Vertical profile of model output in terms of mixing ratios, and (c) vertical profile of model output in terms of precipitation process rates. See text for explanation.

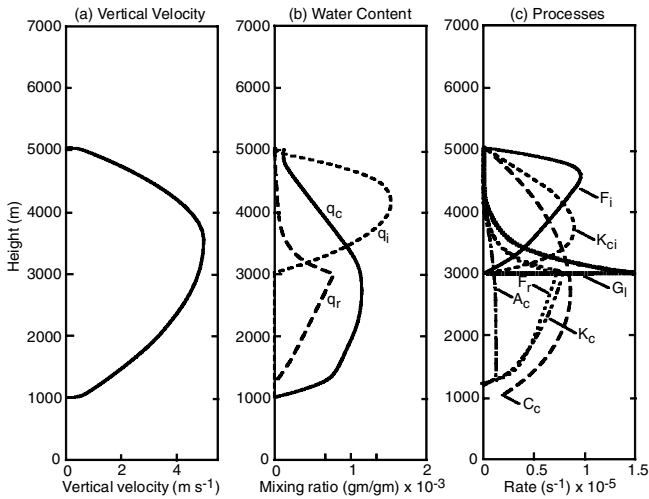


Figure 14. Same as Fig. 13 except for model results using vertical velocity profile with maximum $w = 5 \text{ m s}^{-1}$ and updraught top of 5 km.

The resulting profile of mixing ratio and process rate for the different updraught strengths are generally similar in shape, with the profile corresponding to the 5 m s^{-1} peak updraught having larger magnitude mixing ratios and rates as expected. Other calculations performed (not shown) using a maximum w of 2 m s^{-1} (5 m s^{-1}) and a maximum altitude of 5 km (7 km) showed qualitatively similar results.

The simplicity of the calculation limits our ability to make quantitative interpretations, but some qualitative interpretations can be made. At weak-to-moderate vertical velocities observed in IOP 2b precipitation, the layer 2 km thick above the freezing level contains local maxima in q_i and K_{ci} , indicating that this region is a favourable growth environment for graupel. Medina and Houze (2003) found graupel at these altitudes in

TABLE 2. ESTIMATE OF RELATIVE AMOUNT OF CLOUD WATER CONVERTED TO RAIN WATER IN COLUMN FROM 1 TO 3 km A.G.L. BASED ON VARIOUS INPUTS TO 1D CLOUD MODEL

Maximum vertical velocity w (m s^{-1})	Maximum height z (km)	$\sum q_r / \sum q_c$
2	5	0.15
2	7	0.13
5	5	0.40
5	7	0.36

q_r and q_c are the mixing ratios of rain and cloud water, respectively.

dual polarization radar data obtained by NCAR S-Pol radar in several MAP storms, including IOP 2b. A comparison of the relative rates of K_c below the freezing level and K_{ci} above the freezing level indicates that collection of cloud water by rain and by ice are both important to the growth of precipitation and that neither can be ignored.

Precipitation efficiency is often defined as the ratio of observed rainfall at the surface to computed condensed water, where the latter is deduced using upper-air soundings in inflow air and an estimate of lifting (Smith 1979). An estimate of a quantity related to precipitation efficiency can be made by comparing the column-integrated values of q_r and q_c , e.g. the area under the curves of q_r versus q_c in Figs. 13(b) and 14(b). For simplicity, we examine only the region below the freezing level within cloud (1–3 km altitude) to obtain an estimate of column-integrated rainfall obtained from condensed cloud water. The ratio of areas under the q_r versus q_c curves are shown in Table 2. The source terms (autoconversion and collection) in (8) can be described generically as liquid drop coalescence. Liquid drop coalescence describes processes occurring both within ‘warm clouds,’ i.e. clouds that are warmer than 0°C throughout and incapable of supporting ice-crystal precipitation mechanisms, and within ‘cold clouds’ extending above the 0°C level*. If the assumptions in the 1D model are valid, this calculation implies that liquid drop coalescence in updraughts peaking at 5 m s^{-1} can extract up to $\sim 40\%$ of the condensed cloud water as rain. As previously hypothesized by Browning *et al.* (1975), in order to obtain higher precipitation efficiencies, a combination of both liquid drop coalescence and ice-phase processes is needed.

The profiles in Figs. 13 and 14 show the growth of particles formed and grown entirely within the postulated updraught. An important question is: what is the horizontal distance traversed by hydrometeors growing in and falling out of the updraught cell? For illustration purposes the following calculations assume a horizontal wind speed of 10 m s^{-1} .

An updraught parcel with a w profile corresponding to Fig. 13(a) rising from cell base to cell top would take 40.8 minutes to ascend, which corresponds to a horizontal downwind distance of 24.5 km. For a w profile corresponding to Fig. 14(a), the time to ascend is 12.9 minutes and the horizontal advection is 7.7 km. Thus the particle-growth processes occurring in the cell all take place in a distance less than the ~ 50 –80 km horizontal-scale of the windward side of the Alps near Locarno. A particle (either pre-existing or newly formed in the cell) having grown to precipitation size in the cell would fall from a height of ~ 3.7 km (the height of maximum riming growth) to the surface in about 10 minutes (assuming a fall speed of 6 m s^{-1}), which corresponds to

* Cold clouds predominated during IOP 2b. Our 1D model reflects this observation by including an ice layer. Use of the term ‘warm rain’ to describe liquid drop coalescence within cold clouds is a misnomer.

~6 km downwind distance. This distance is also well within the horizontal-scale of the windward slopes of the southern Alps.

6. CONCLUSIONS

The University of Washington OPRA obtained vertically pointing S-band Doppler-radar data at high temporal resolution (1 s) and high spatial resolution* ($\sim 3 \times 10^{-3} \text{ km}^3$ sample volume near the altitude of the melting layer) at Locarno-Monti during MAP. Analysis of OPRA data obtained during MAP IOPs 2b and 8 indicates that fallstreaks are nearly ubiquitous in a wide range of precipitation intensities. Several dynamical mechanisms can yield small-scale inhomogeneities in the microphysical structure of a storm associated with fallstreaks. In unstable environments, such as IOP 2b, convective overturning was probably the dominant mechanism. In more stable environments, such as IOP 8, shear-driven turbulence as observed near the 0°C level (Steiner *et al.* 2003) probably played a role in fallstreak formation. Higher-rain-rate pulses >10-minutes duration, associated with convective cells evident in coarser-resolution scanning radar data, manifested as an increased frequency and intensity of fallstreaks each <5-minutes duration in the OPRA data. A subset of the fallstreaks had sufficient magnitude in reflectivity to indicate a clear connection across the melting layer from the snow to the rain region. Terminal velocities of up to $\sim 8 \text{ m s}^{-1}$ were estimated within fallstreaks in the rain region (Fig. 9(c)).

A distinct melting layer, and hence unambiguous evidence of precipitation-sized ice, was present in most of the samples of OPRA data obtained during IOPs 2b and 8 with surface rainfall $\gtrsim 1$ and $\lesssim 36 \text{ mm h}^{-1}$. The width and intensity of the reflectivities within the melting layers varied with surface rain rate. However, the relative decrease in Z between the local melting-layer maxima and the peak Z in rain 1 km below remained remarkably consistent at $\sim 8\text{--}10 \text{ dB}$ for a wide range of surface precipitation rates (e.g. Figs. 3 and 6). For high rain rates $\gtrsim 36 \text{ mm h}^{-1}$, neither discernible fallstreaks nor a distinct narrow melting layer were evident (e.g. Fig. 5). Both structures may have been diffused in the presence of strong convective overturning within the heavy rain.

An estimation of characteristics of the vertical air velocity profile within precipitating cloud was made both in rain and in snow regions using the observed radar parameters. In rain regions reflectivity-weighted fall speed, derived from the observed reflectivity with assumptions about the RSDS and an empirical fall speed to diameter relation, was subtracted from the observed Doppler velocity to yield an estimated w . In snow regions a lower bound on maximum updraught w was estimated from the observed maximum Doppler velocity. Using these methods on data from IOP 2b, typical peak vertical velocities within an updraught were estimated to be 2 to 5 m s^{-1} .

Plausible parabolic vertical velocity profiles with maximum velocities between 2 and 5 m s^{-1} were input into a simple calculation based on Kessler's 1D water-continuity model (section 5(b), Figs. 13 and 14). These calculations yielded local maxima in q_i and K_{ci} within 2 km of the freezing level. These conditions constitute a favourable environment for graupel formation, and their altitude corresponds to the layer where graupel was observed in NCAR S-Pol dual polarization radar data during IOP 2b (Medina and Houze 2003).

Studies in the 1950s, 60s and 70s indicated that in conditions of deep moist flow over a mountain range the total column (ice + liquid drop coalescence) precipitation

* The OPRA-resolution volume in units of km^3 corresponding to a particular range gate can be estimated as the volume of a cylinder where h is the height a.g.l. in km with $Volume = 0.150 \frac{\pi}{4} (h \sin(4.3^\circ))^2$.

efficiencies within deep orographic rain are $\sim 70\%$ or more (see review by Smith 1979). Browning *et al.* (1975) suggested that a combination of both liquid-water coalescence and ice-phase processes are needed to obtain high precipitation efficiencies in orographic precipitation. Our 1D model results further indicate the importance of processes both below and above the freezing level in the efficient production of precipitation over windward slopes. We find that the rates of collection and riming are comparable, and make significant contributions to the growth of precipitation by accretion within the small-scale embedded updraughts (Figs. 13 and 14). An estimate of a quantity related to precipitation efficiency based on the 1D model calculation indicates that liquid-water coalescence (autoconversion and collection) processes associated with updraughts with a peak w of 5 m s^{-1} can yield column-integrated rain water constituting $\leq 40\%$ of column-integrated cloud water*. These results suggest that within typical small-scale embedded updraughts associated with MAP storms, liquid-water coalescence alone will be insufficient to yield the high precipitation efficiencies often observed in orographic precipitation.

ACKNOWLEDGEMENTS

The authors gratefully acknowledge the work of several people in the successful deployment of University of Washington's OPRA radar during MAP. Grant Gray designed and built OPRA and oversaw its installation in Locarno. Steve Domonkos built OPRA's antenna platform. Katherine Pearl and Don Kaydk worked on instrument testing, preparing for field deployment, and instrument installation at Locarno. Jürg Joss and Urs Germann of the Swiss Meteorological Agency mentored the OPRA equipment during its stay in Locarno and worked closely with the authors on analysis of the data. Mel Nordquist and Nancy White of the Eureka, CA National Weather Service Forecast Office, and Clifford Spooner of North Bend, WA graciously allowed testing at their facilities and watched over the instrumentation. David Spencer toiled on a wide variety of tasks associated with the test deployments in California and Washington. Candace Gudmundson edited the manuscript and Kay Dewar worked on the figures. Additionally the authors would like to thank Chih-Chieh (Jack) Chen for his software for the 1D model and Martin Hagen for his disdrometer data. This work was supported by NSF grants ATM-9409988, ATM-9817700, and ATM-0121963.

APPENDIX

One-dimensional cloud-model description

The following equations were used in the 1D water-continuity model after Kessler (1969), Ogura and Takahashi (1971), Ferrier (1988), and Houze (1993, his section 3.6). With the exception of (A.4), Ogura and Takahashi (1971) equations and coefficients were used. Equation (A.4) was derived following Ferrier (1988) using a collection efficiency of unity and using Locatelli and Hobbs's (1974, their Table 1) fall speed for conical graupel of $V_{fi} = 1.2D_m^{0.65}$ in m s^{-1} where D_m is the maximum diameter of the particle in mm.

$$A_c = \tilde{\alpha}(q_c - a_t), \quad (\text{A.1})$$

$$K_c = \tilde{\beta}q_cq_r^{0.875}, \quad (\text{A.2})$$

$$F_r = q_rV_t/b. \quad (\text{A.3})$$

* Calculation of the equivalent quantity related to ice processes is beyond the scope of the current study.

TABLE A.1. VALUES OF COEFFICIENTS USED IN 1D WATER-CONTINUITY CALCULATION

Coefficient	Value
$\tilde{\alpha}$	0.001, if $q_c > a_t$ 0 otherwise
a_t	0.0005
β	0.02
β'	3.066
$\tilde{\beta}$	2.19
V_t	3 m s ⁻¹
V_{ti}	6 m s ⁻¹

For $T < 0^\circ\text{C}$,

$$K_{ci} = \beta' q_c q_i^{0.9125}, \quad (\text{A.4})$$

$$F_i = q_i V_{ti}/b, \quad (\text{A.5})$$

$$G_1 = \beta q_r. \quad (\text{A.6})$$

The value of b for a specific level i is calculated iteratively from the temperature and pressure, and is used to account for the varying density of air with height. Other coefficient values are given in Table A.1.

$$b(i) = b(i-1)[(T(i) * P(i-1))/\{T(i-1) * P(i)\}]^{1/3}. \quad (\text{A.7})$$

REFERENCES

- Atlas, D., Srivastava, R. C. and Sekhon, R. S. 1973 Doppler-radar characteristics of precipitation at vertical incidence. *Rev. Geophys. Space Phys.*, **11**, 1–35
- Austin, P. M. and Houze Jr, R. A. 1972 Analysis of the structure of precipitation patterns in New England. *J. Appl. Meteorol.*, **11**, 926–935
- Berry, E. X. and Pranger, M. R. 1974 Equations for calculating the terminal velocities of water drops. *J. Appl. Meteorol.*, **13**, 108–113
- Bougeault, P., Binder, P., Buzzi, A., Dirks, R., Kuettner, J., Houze, R., Smith, R. B., Steinacker, R. and Volkert, H. 2001 The MAP Special Observing Period. *Bull. Am. Meteorol. Soc.*, **82**, 433–462
- Braun, S. A., Houze Jr, R. A. and Smull, B. F. 1997 Airborne dual-Doppler observations of an intense frontal system approaching the Pacific northwest coast. *Mon. Weather Rev.*, **125**, 3131–3156
- Bringi, V. N. and Chandrasekar, V. 2001 *Polarimetric Doppler weather radar: Principles and applications*. Cambridge University Press, Cambridge, UK
- Browning, K. A., Pardoe, C. and Hill, F. F. 1975 The nature of orographic rain at wintertime cold fronts. *Q. J. R. Meteorol. Soc.*, **101**, 333–352
- Chandrasekar, V. and Bringi, V. N. 1987 Simulation of radar reflectivity and surface measurements of rainfall. *J. Atmos. Oceanic Technol.*, **4**, 464–478
- Churchill, D. D. and Houze Jr, R. A. 1984 Development and structure of winter monsoon cloud clusters on 10 December 1978. *J. Atmos. Sci.*, **41**, 933–960
- Ferrier, B. S. 1988 'One-dimensional time-dependent modeling of squall-line convection'. PhD thesis, University of Washington
- Frei, C. and Schär, C. 1998 A precipitation climatology of the Alps from high-resolution rain-gauge observations. *Int. J. Climatol.*, **18**, 873–900
- Gossard, E. E. 1988 Measuring drop-size distributions in clouds with a clear-air-sensing Doppler radar. *J. Atmos. Ocean Technol.*, **5**, 640–649
- Gossard, E. E., Strauch, R. G. and Rogers, R. R. 1990 Evolution of droplet size distributions in liquid precipitation observed by ground-based Doppler radar. *J. Atmos. Ocean Technol.*, **7**, 815–828

- Gunn, R. and Kinzer, G. D. 1949 The terminal velocity of fall for water droplets in stagnant air. *J. Meteorol.*, **6**, 243–248
- Hanesch, M. 1999 'Fall velocity and shape of snowflakes'. Ph.D. dissertation, ETH, Zurich
- Hogan, R. J., Field, P. R., Illingsworth, A. J., Cotton, R. J. and Choulaton, T. W. 2002 Properties of embedded convection in warm-frontal mixed-phase cloud from aircraft and polarimetric radar. *Q. J. R. Meteorol. Soc.*, **128**, 451–476
- Houze Jr, R. A. 1993 *Cloud dynamics*. Academic Press, San Diego, USA
- Houze Jr, R. A., Kuettner, J. and Smith, R. B. 1998 'Mesoscale Alpine Programme. US overview document and experimental design'. Available from MAP US Project Office, UCAR (http://www.joss.ucar.edu/joss_psg/projects/map)
- Houze Jr, R. A., James, C. N. and Medina, S. 2001 Radar observations of precipitation and airflow on the Mediterranean side of the Alps: Autumn 1998 and 1999. *Q. J. R. Meteorol. Soc.*, **127**, 2537–2558
- Jameson, A. R. and Kostinski, A. B. 2000 Observations of hyperfine clustering and drop size distribution structures in three-dimensional rain. *J. Atmos. Sci.*, **57**, 373–388
- Joss, J. and Gori, E. G. 1978 Shapes of raindrop size distributions. *J. Appl. Meteorol.*, **17**, 1054–1061
- Kessler, E. 1969 *On the distribution and continuity of water substance in atmospheric circulation*. Meteorological Monographs, Vol. 10, No. 32. American Meteorological Society, Boston, USA
- Locatelli, J. D. and Hobbs, P. V. 1974 Fall speeds and masses of solid precipitation particles. *J. Geophys. Res.*, **79**, 2185–2197
- Marshall, J. S. and Palmer, W. M. 1948 The distribution of raindrops with size. *J. Meteorol.*, **5**, 165–166
- Medina, S. and Houze Jr, R. A. 2003 Air motions and precipitation growth in Alpine storms. *Q. J. R. Meteorol. Soc.*, **129**, 345–371
- Ogura, Y. and Takahashi, T. 1971 Numerical simulation of the life cycle of a thunderstorm cell. *Mon. Weather Rev.*, **99**, 895–911
- Rotunno, R. and Ferretti, R. 2003 Orographic effects on rainfall in MAP cases IOP 2b and IOP 8. *Q. J. R. Meteorol. Soc.*, **129**, 373–390
- Smith, R. B. 1979 The influence of mountains on the atmosphere. *Adv. Geophys.*, **21**, 87–230
- Smith, P. L., Liu, Z. and Joss, J. 1993 A study of sampling variability effects in raindrop size observations. *J. Appl. Meteorol.*, **32**, 1259–1269
- Steiner, M., Houze Jr, R. A. and Yuter, S. E. 1995 Climatological characterization of three-dimensional storm structure from operational radar and rain gauge data. *J. Appl. Meteorol.*, **34**, 1978–2007
- Steiner, M., Bousquet, O., Houze Jr, R. A., Smull, B. F. and Mancini, M. 2003 Airflow within major Alpine river valleys under heavy rainfall. *Q. J. R. Meteorol. Soc.*, **129**, 411–431
- Ulbrich, C. W. 1983 Natural variations in the analytical form of the raindrop size distribution. *J. Clim. Appl. Meteorol.*, **22**, 1764–1775
- Waldvogel, A. 1974 The N_0 jump in raindrop spectra. *J. Atmos. Sci.*, **31**, 1067–1078
- White, A. B., Neiman, P. J., Ralph, F. M., Kingsmill, D. A. and Persson, P. O. G. 2003 Coastal orographic rainfall processes observed by radar during the Californian Landfalling Jets Experiment. *J. Hydrometeorol.*, in press
- Wüest, M., Schmid, W. and Joss, J. 2000 'Coupling between riming and the dynamics of precipitating clouds'. Pp. 421–424 in Proceedings of the 13th international conference on clouds and precipitation, Reno, NV. American Meteorological Society, Boston, USA
- Yuter, S. E. and Houze Jr, R. A. 1995 Three-dimensional kinematic and microphysical evolution of Florida cumulonimbus, Part II: Frequency distributions of vertical velocity, reflectivity, and differential reflectivity. *Mon. Weather Rev.*, **123**, 1941–1963
- Zeng, Z., Yuter, S. E., Houze Jr, R. A. and Kingsmill, D. E. 2001 Microphysics of the rapid development of heavy convective precipitation. *Mon. Weather Rev.*, **129**, 1882–1904